Cryogenics 148 (2025) 104074

Contents lists available at ScienceDirect

Cryogenics

journal homepage: www.elsevier.com/locate/cryogenics

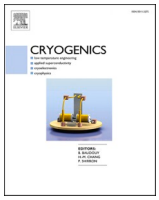

Performance evaluation of the magnetothermal properties of GGG and $ErAl_2$ packed beds at cryogenic temperatures☆

Carlos Hernando [a,b,*], Javier Munilla [b,c], Luis García-Tabarés [c]

[a] CYCLOMED TECHNOLOGIES, 28043 Madrid, Spain
[b] Comillas Pontifical University, 28015 Madrid, Spain
[c] Centro de Investigaciones Energéticas, Medioambi- entales y Tecnológicas (CIEMAT), 28040 Madrid, Spain

ARTICLE INFO

Keywords:
Magnetic refrigeration
Cryogenics
Numerical modeling
Experimental validation

ABSTRACT

The development of high-temperature superconductors (HTS) has highlighted the need for advanced cryocooling technologies capable of achieving high efficiency at extremely low temperatures. Among the various cooling techniques, magnetic refrigeration has emerged as a promising method due to its potential for high Carnot efficiency at temperatures corresponding to liquid helium and liquid hydrogen. A test stand has been developed to evaluate the heat transfer dynamics and the magnetocaloric effect of packed beds of magnetocaloric materials. This article presents the results and analysis of the testing of two magnetocaloric materials, Erbium Aluminum II ($ErAl_2$) and Gadolinium Gallium Garnet (GGG), in the range of 4.2–20 K. The recorded temperatures measurements are compared with numerical predictions for different fluid mass flow rates, temperatures, and magnetic field values. Insights gained from the testing will be used to develop a scaled magnetic refrigerator based on both materials.

1. Introduction

Refrigeration systems play a crucial role in a wide array of applications, spanning from near-ambient temperatures of 300 K down to the extreme cold of liquid helium, approaching absolute zero [1].

Cryocoolers have been the primary devices for reaching these temperatures, and they had significant advancements during the last 20 years of the 20th century. Despite improvements in cooling power and reliability, cryocoolers still face limitations in terms of cost and Carnot efficiency [2]. These constraints have spurred ongoing research into alternative refrigeration methods. One promising approach is magnetic refrigeration [3], which leverages the magnetocaloric effect (MCE) to achieve high Carnot efficiencies due to its reversible nature [4].

To effectively model magnetic refrigerators, it is essential to understand the underlying heat transfer and fluid dynamics mechanisms. While correlations developed for ambient temperature processes [5] have been successfully applied down to temperatures as low as 70 K [6], there is a scarcity of validated correlations for heat transfer and fluid dynamics at liquid helium temperatures.

This study focuses on the development of a numerical model tailored to magnetic refrigeration and its experimental validation using a custom-built test stand. The article is divided in four sections: the first section is dedicated to the development of the numerical model, including the governing equations, the numerical scheme and the most relevant fluid and material properties, the second section describes the experimental test stand and the adopted testing procedure, the third section provides the results of the tests and a discussion on how the model fits the measured data. Finally, some concluding remarks are provided in the last section.

2. Numerical modeling

2.1. Governing equations

It is usual for the modelling of magnetic refrigeration system to develop one-dimensional (1D) models, since they are computationally efficient and allows the exploration and optimization of different parameters of the cooling system.

For room temperature applications, several 1D models have been developed [7], where an incompressible fluid such as water is often used as the heat transfer medium, simplifying the mass conservation equation and reducing the momentum equation to a balance between the pressure

☆ This article is part of a special issue entitled: 'HTS Cooling 2024' published in Cryogenics.

* Corresponding author at: CYCLOMED TECHNOLOGIES, 28043 Madrid, Spain.
E-mail address: c.hernando@cyclomed.tech (C. Hernando).

https://doi.org/10.1016/j.cryogenics.2025.104074
Received 18 December 2024; Received in revised form 13 March 2025; Accepted 3 April 2025
Available online 7 April 2025

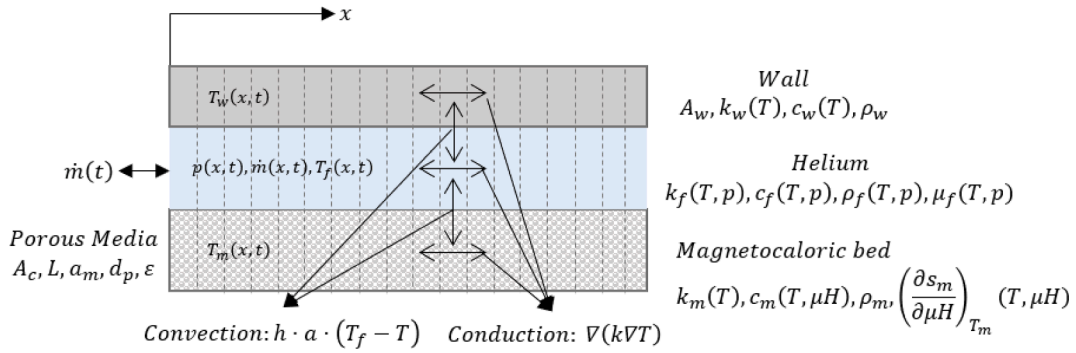

Fig. 1. Conceptual drawing of a 1D AMR model showing the important parameters.

gradient and drag forces. This leads to a model focused on time-dependent thermal energy equations for both the fluid and solid components.

At cryogenic temperatures, the working fluid is typically a compressible gas like helium, which significantly affects the modeling approach. Due to helium's compressibility, its density varies significantly at cryogenic temperatures, especially below 20 K. Therefore, accurate modeling at cryogenic temperatures requires solving the full set of nonlinear compressible equations governing fluid motion and energy transfer within the porous structure.

The development of such models proves to be challenging as reported by [5,8], and certain numerical methodologies are not valid for the computation of such models. In this work a similar approach to previous developments has been adopted with slight differences, such as the inclusion of the housing wall, that will be evident along with the description of the model.

For the developed 1D model the following assumptions are established:

- Magnetocaloric effect is a reversible process, and no hysteresis effect is accounted for in the model.
- The applied magnetic field (in the empty air gap of the magnetic field source) is equal to the internal magnetic field in the magnetocaloric material.
- The solid within the regenerator is uniformly distributed with no edge effects. No flow leakage or flow bypassing occurs. Any dead volume (the volume between the entry/exit of the AMR and valve/flow divider) is neglected.

Having established the main assumptions, we continue to describe the physical system model. The general laws that describe the undergoing physics are: first, the continuity equation which describes the conservation of mass of the working fluid within the regenerator, which is given by:

$$\frac{d(\varepsilon\rho_f)}{dt} + \nabla(\rho_f u) = 0 \tag{1}$$

where ρ_f is the density of the fluid, ε is the porosity, and u is the fluid velocity.

Second, the conservation of the fluid's momentum, in which viscous stresses and the convective terms are omitted. Therefore, the momentum is given by:

$$\frac{1}{\varepsilon}\frac{d(\rho_f u)}{dt} = \nabla p - F_d \tag{2}$$

F_d is the drag force exerted by the solid porous medium on the fluid. And third, the energy balance equation for a compressible fluid is given by:

$$\frac{d(\rho_f E)}{dt} + \nabla(u\rho_f h) + \frac{1}{\varepsilon^2}\nabla\left(\frac{u\rho_f u^2}{2}\right) = \nabla(k_f \nabla T_f) - h_m a_m (T_f - T_m) - h_w a_w (T_f - T_w) \tag{3}$$

where E is the total energy of the fluid, i.e., the sum of the internal and kinetic energy, h is the enthalpy of the fluid, k_f is the effective thermal conductivity of the fluid due to axial dispersion, h_m and h_w are the heat transfer coefficient between fluid-magnetocaloric and fluid-wall respectively, a_m and a_w are the specific surface area between fluid-magnetocaloric and fluid-wall, and T_f, T_m, T_w are the temperatures of the fluid, magnetocaloric and wall, respectively.

The thermal equation for the magnetocaloric material is:

$$(1-\varepsilon)\rho_m\left(c_m\frac{\partial T_m}{\partial t} + T_m\left(\frac{\partial s_m}{\partial \mu H}\right)_{T_m}\frac{\partial \mu H}{\partial t}\right) = \nabla\cdot\left(k_m^{eff}\nabla T_m\right) + h_m a_m (T_f - T_m) \tag{4}$$

where ρ_m is the density of the material, c_M is the specific heat capacity, s_m is the specific entropy, k_m^{eff} is the axial effective thermal conductivity of the solid and $\mu\ H$ is the applied magnetic field.

Finally, the thermal equation for the wall is:

$$\rho_w\left(c_w\frac{\partial T_w}{\partial t}\right) = \nabla\cdot(\mathrm{k_w}\nabla T_w) + h_w a_w (T_f - T_w) + Q_{loss} \tag{5}$$

where ρ_w is the density of the wall, c_w is the specific heat capacity of the wall, $\mathrm{k_w}$ is the axial thermal conductivity. The term Q_{loss} represent heat losses to the ambient.

Fig. 1 shows a schematic of the 1D model, it includes the heat transfer fluid, gas helium in this case, the magnetocaloric material, $ErAl_2$ or GGG, and the wall housing of the packed bed.

2.2. Numerical methodology

Eqs. 1–5 are expanded, the velocity is substituted by the mass flow rate through the following relation: $\dot{m} = \rho_f u A$, and the density partial derivative term of the mass conservation equation is expanded by the chain rule to their temperature and pressure components. This modification yields the following system of equations, with 5 variables ($p, \dot{m}, T_f, T_m, T_w$) and 5 equations:

$$\left(\frac{d\rho_f}{dp}\frac{dp}{dt}+\frac{d\rho_f}{dT}\frac{dT}{dt}\right)=-\frac{1}{\varepsilon AL}\frac{d\dot{m}}{d\bar{x}} \tag{6}$$

$$\frac{1}{\varepsilon AL}\frac{d\dot{m}}{dt}=\frac{dp}{d\bar{x}}-F_d \tag{7}$$

$$m_f c_f\frac{dT}{dt}=\frac{A_f k_f}{L}\frac{d^2T}{d\bar{x}^2}-\dot{m}c_f\frac{dT}{d\bar{x}}-h_m a_m\left(T_f-T_m\right)-h_w A_w\left(T_f-T_w\right)+\frac{dp}{d\bar{x}}\frac{\dot{m}}{\rho_f} \tag{8}$$

$$m_m\left(c_m\frac{\partial T_m}{\partial t}\right)=\frac{A_m k_m^{eff}}{L}\frac{d^2T}{d\bar{x}^2}+h_m a_m\left(T_f-T_s\right)-m_m T_m\left(\frac{\partial s_m}{\partial \mu H}\right)_{T_m}\frac{\partial \mu H}{\partial t} \tag{9}$$

$$m_w c_w\frac{\partial T_w}{\partial t}=\frac{A_w k_w^{eff}}{L}\frac{d^2T_w}{d\bar{x}^2}+h_w a_w\left(T_f-T_w\right)+Q_{loss} \tag{10}$$

Where the dimensionless variable $\bar{x}=x/L$ is used. The heat transfer, pressure and axial conductivities adopted correlations in this study are addressed in the following section.

The system of partial differential equations (PDEs) is solved in MATLAB with the pde1dm solver. This solver is a variation of the MATLAB standard pdepe solver with certain modifications and upgrades. Both are based on the work of Skeel and Berzin [9]. Both programs are designed to handle systems of PDEs in one spatial dimension and time, using a method of lines (MOL) approach for numerical solution. This method is applied to systems of PDEs in the form:

$$c\left(x,t,u,\frac{\partial u}{\partial x}\right)\frac{\partial u}{\partial t}=x^{-g}\frac{\partial}{\partial x}\left(x^g f\left(x,t,u,\frac{\partial u}{\partial x}\right)\right)+s\left(x,t,u,\frac{\partial u}{\partial x}\right) \tag{11}$$

Where $u(x,t)$ represents the solution vector, containing the dependent variables (fluid and magnetocaloric temperature), $c\left(x,t,u,\frac{\partial u}{\partial x}\right)$ is the time-dependent coefficient matrix, $f\left(x,t,u,\frac{\partial u}{\partial x}\right)$ denotes the flux vector, $s\left(x,t,u,\frac{\partial u}{\partial x}\right)$ denotes the source terms, and g is a geometric parameter indicating the symmetry of the problem, which in this case takes the value of 0.

The method of lines first discretizes the spatial variable while leaving the time derivative continuous. The spatial derivatives are approximated using finite-difference schemes. In that way the PDE is converted into an ordinary differential equation (ODE) at each point of the grid.

Once the system of PDEs has been discretized in space, it employs an ODE solver for the time integration of the resulting system of ODEs. The ODE system can be written as:

$$M\frac{dU}{dt}=F(U,t) \tag{12}$$

where U is the vector of all spatially discretized solution components, M is the mass matrix, and $F(U,t)$ represents the fluxes and source terms in the discretized spatial form.

The time-stepping methods used in both solvers are based on the ODE15s solver, which is well-suited for stiff problems. This solver is a variable-step, variable-order (VSVO) method that adapts both the step size and the order of the solution to efficiently handle stiffness. The solver uses backward differentiation formulas (BDFs), which are implicit methods known for their stability properties, crucial for accurately solving the highly stiff ODEs arising from AMR systems.

The most relevant upgrades of pde1dm solver over traditional pdepe is that it allows for spatial vectorization during resolution which significantly improves computation time, and allows the computation of non-diagonal "c" matrices, which is relevant to this study as Equation (6) has one non-diagonal term.

2.3. Experimental correlations: Heat transfer, pressure drop and thermal conductivity

The transport and heat transfer phenomena are significantly influenced by fluid flow characteristics, necessitating the determination of the Reynolds number:

$$Re_{dp}=\frac{d_p\cdot\dot{m}_f}{(1-\varepsilon)A\cdot\mu_f} \tag{13}$$

where d_p is the particle diameter, and μ_f represents the dynamics viscosity of the fluid, A denotes the free flow area, and ε the porosity, calculated as:

$$\varepsilon=\frac{VoidVolume}{TotalVolume} \tag{14}$$

2.3.1. Heat transfer correlations

The heat transfer between the fluid and the magnetocaloric is modeled with a heat transfer coefficient (h_m), which can be derived from empirical Nusselt correlations. Wakao and Kaguei [10] suggest the following empirical correlation valid for all Reynolds values:

$$Nu_{dp}=\frac{d_p\cdot h_m}{k_f}=2+1.1\cdot Pr^{\frac{1}{3}}\cdot Re_{dp}^{0.6} \tag{15}$$

where h_c the heat transfer coefficient, k_f the thermal conductivity of the fluid, Pr the Prandtl number.

Heat transfer between the fluid and the wall is modeled in an analogous manner [11]:

$$Nu_{dp}=0.17\cdot Re_{dp}^{0.17} \tag{16}$$

2.3.2. Pressure correlations

The parameter F_d in Eq. (2.27) is the drag force exerted by the magnetocaloric material in the fluid. For the purposes of this study F_d is computed under the Darcy-Forcheimer relation for a packed bed filled with spheres of uniform diameter:

$$F_d=\frac{\mu}{K}u+\frac{c_f\rho_f}{\sqrt{K}}|u|u \tag{17}$$

where K and c_f are established in order to satisfy Ergun correlation [12]:

$$K=\frac{\varepsilon^3 d_p^2\varnothing^2}{150(1-\varepsilon)^2} \tag{18}$$

$$c_f=\frac{1.75\varnothing}{\sqrt{150}\varepsilon^{\frac{3}{2}}} \tag{19}$$

where $\varnothing$ the shape factor is defined as the ratio between the specific area of a regenerator made of spherical particles to the specific area of the regenerator bed under consideration.

2.3.3. Effective thermal conductivity

The fluid mixes along the direction of the flow due to the dispersion caused by the packed bed. This term can be treated as an axial conduction term. The total effective conductivity is a sum of the static thermal conductivity, and the axial conductivity caused by the dispersion. According to Kaviani [13], the total effective conductivity can be expressed as:

$$k_{eff}=k_{static}+k_f D^d \tag{20}$$

Hadley [14] presents a correlation for the static fluid conductivity in a porous structure:

Table 1
Magnetic refrigeration prototypes based on GGG operating between 4.2–20 K

Authors	Year	Cycle	Magnetic source	MCM	Frequency (f)	T. Cooling (T_{cold})	T. Span (ΔT)	Cooling power ($Q_{cooling}$)	Ref.
Los Alamos group	1985	Carnot	SM (6 T)	GGG	<0.1Hz	5 K	6 K	~0.05 W	[16]
Toshiba & Tokyo Tech. group	1984	Carnot	SM (5.6 T)	GGG	<0.1Hz	4.2 K	>10 K	<3 W	[17]
Toshiba & Tokyo Tech. group	1986	Carnot	SM (4.5 T)	GGG	0.38 Hz	4.2 K	>10 K	0.95 W	[18]
MIT group	1997	GM/AMR	SM (4 T)	GGG	0.1 Hz	5.6 K	~10 K	0.36 W	[19]

$$k_{static}=k_f\left[(1-\alpha_0)\frac{\varepsilon f_0+\frac{k_m}{k_f(1-\varepsilon f_0)}}{1-\varepsilon(1-f_0)+\frac{k_m}{k_f\varepsilon(1-f_0)}}+\alpha_0\frac{2\left(\frac{k_m}{k_f}\right)^2(1-\varepsilon)+\frac{(1+2\varepsilon)k_m}{k_f}}{\frac{(2+\varepsilon)k_m}{k_f}+1-\varepsilon}\right] \quad (21)$$

$$f_0=0.8+0.1\varepsilon$$

$$log\alpha_0=-4.898\varepsilon, 0\le\varepsilon\le 0.0827$$

$$log\alpha_0=-0.405-3.154(\varepsilon-0.0827), 0.0827\le\varepsilon\le 0.298$$

$$log\alpha_0=-1.084-6.778(\varepsilon-0.298), 0.298\le\varepsilon\le 0.580$$

For the dispersion coefficient the model presented by Kaviany is used:

$$D^d=\varepsilon\frac{3}{4}Pe_f \quad (22)$$

where Pe_f is the Peclet number defined as $Pe_f = Re_f Pr_f$.

3. Material properties

3.1. Fluid properties

The primary fluid utilized in this study is Helium-4, whose properties at low temperatures exhibit significant non-ideal behavior. Accurately representing these properties is essential for ensuring the reliability of the model. In this work, the thermodynamic properties of Helium-4 are determined using bicubic spline interpolation applied to tabulated data as functions of internal energy and pressure. This approach offers a significant advantage over linear interpolation, where the second derivative is discontinuous at each data point and zero within each interval. From a thermodynamic perspective, this distinction is critical because higher-order derivatives of thermodynamic properties ensure consistency with the second law of thermodynamics. Specifically, these derivatives preserve the concavity of the fundamental relation with respect to energy and the convexity of the energy relation with respect to entropy, thereby maintaining thermodynamic stability.

These tables are constructed using a MATLAB code using the database provided by the NIST [15]. The helium property tables constructed in this fashion include: density, enthalpy, entropy, viscosity, Prandlt number, thermal conductivity and Joule Thomson coefficient. Any other properties or property derivatives which are required can be obtained from this set of properties or their derivatives.

3.2. Magnetocaloric properties

Two magnetocaloric materials have been selected for the analysis and development of an experimental demonstrator: $ErAl_2$ and gadolinium gallium garnet (GGG).

GGG is a straightforward choice, as it has been the most widely used material for cryogenic applications and is a guarantee for evaluating the technology. A recompilation of some of the most relevant magnetic refrigeration prototypes utilizing GGG and operating in 4.2–20 K range are summarized in Table 1.

Other GGG prototypes developed for operating at below liquid Helium (4.2 K) temperatures are from MIT Cryogenic Engineering Laboratory [20], and research groups in Grenoble [21] and Los Alamos [22].

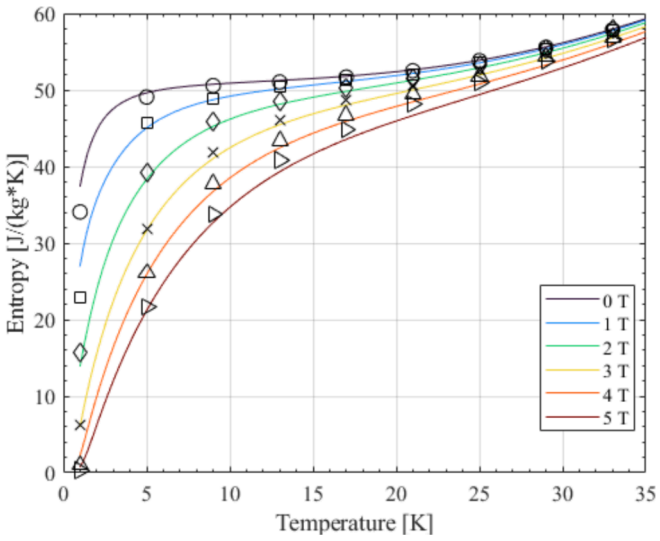

Fig. 2. Entropy of GGG as a function of temperature and magnetic field; in solid lines the results from the theoretical model, and the markers represent experimental data.

On the other hand, a $REAl_2$ compound such as $ErAl_2$ was selected. The main reason for this selection was the higher Curie temperature, around 12 K, its high relative cooling power in the 4.2–20 K range [23], and the possibility of acquiring high quality samples from a reliable supplier at a reasonable price.

The properties needed to define the magnetocaloric material behaviour in a magnetic refrigeration stage are specific heat, entropy, and thermal conductivity, which are dependent on temperature and magnetic field. These properties can be reduced to entropy and thermal conductivity, as the specific heat can be expressed as a function of temperature and entropy: $c_p = T\frac{dS}{dT}$.

In fact, adopting this expression, and having consistent datasets is essential to ensure a consistent solution.

The procedure reported by Murphy [24], which adopts the method proposed by Price and Mastrup [25], has been adopted to compute the properties of GGG. The resulting entropy of GGG from this method is shown in Fig. 2. The model has already been validated against experimental data from their own measurements. In this case, in Fig. 2, the model data is compared against the experimental data from another source [26]. The model fits very well, although there are certain discrepancies in the high fields and high temperature regions.

Fig. 3 shows the derived properties of GGG as function of temperature and magnetic field: the entropy change, and specific heat.

The theoretical model for computing the magnetothermodynamic properties of $ErAl_2$ is adopted from Oliveira et al [23]. Based on this model, the entropy of $ErAl_2$ for the easy direction <1,1,1> is shown in Fig. 4. In the present study an average entropy of three crystallographic directions: <1,1,1>, <1,1,0>, and <1,0,0> was used for the numerical model. It is noteworthy to highlight that the magnetic field represented in the following figures is the externally applied magnetic field.

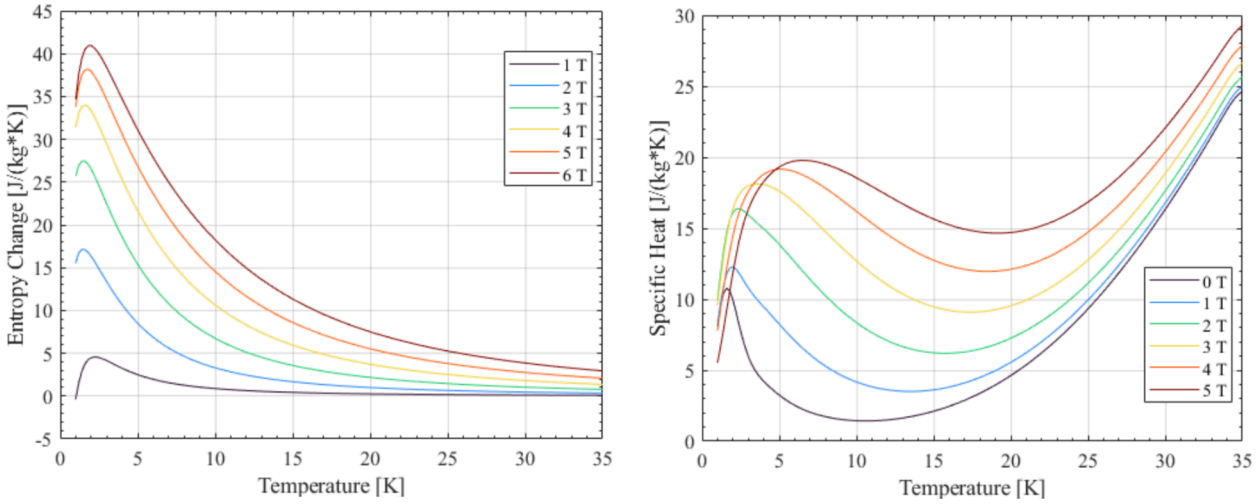

Fig. 3. Entropy change (left) and specific heat (right) of GGG as a function of temperature and magnetic field.

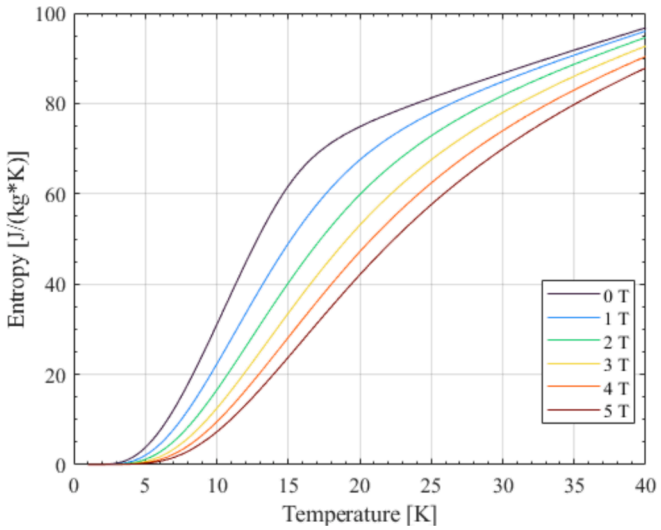

Fig. 4. Entropy of $ErAl_2$ derived from the numerical model.

In this case the specific heat is compared against experimental data from another literature source [27]. Fig. 5 shows the model and experimental results comparison for the specific heat (left), and the resulting entropy change (right). The model behaves reasonably well for values below 10 K, but certain discrepancies arise near the Curie Temperature. In fact, certain discrepancies among experimental data has already been reported in [27,28].

For the thermal conductivity of both materials, GGG and $ErAl_2$, only its temperature dependence has been used as there is limited information in the literature about their magnetic field dependence. The values used were reported in [29].

4. Experimental method

4.1. Experimental test stand

Fig. 6 presents a schematic of the experimental system, which is described with more detail in [30]. The pumping circuit is located at ambient temperature. A mechanical pump from KNF which is helium compatible was used. The pump is oil free, with low leakage and low vibration. The pressure and mass flow of the system are controlled with two mass flow controllers (MFC), MFC1 and MFC2 in Fig. 6. Before entering the cryostat, side there are three manual valves (MV) which control the flow direction inside the cryostat, allowing the testing of two

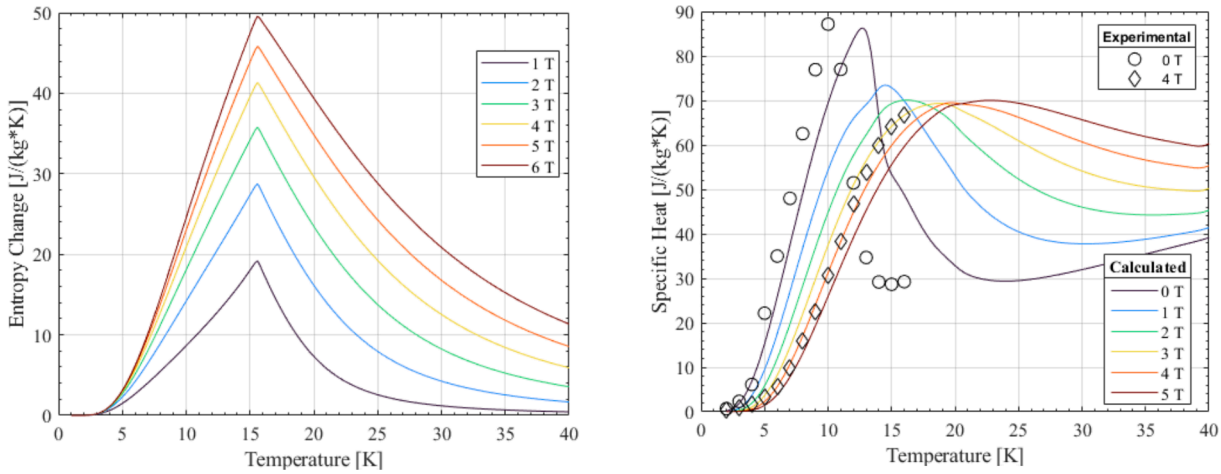

Fig. 5. Entropy change as function of temperature and magnetic field (left). Specific heat of $ErAl_2$ as a function of temperature and magnetic field, solid lines represent model results, while markers represent data obtained from the literature [27] (right).

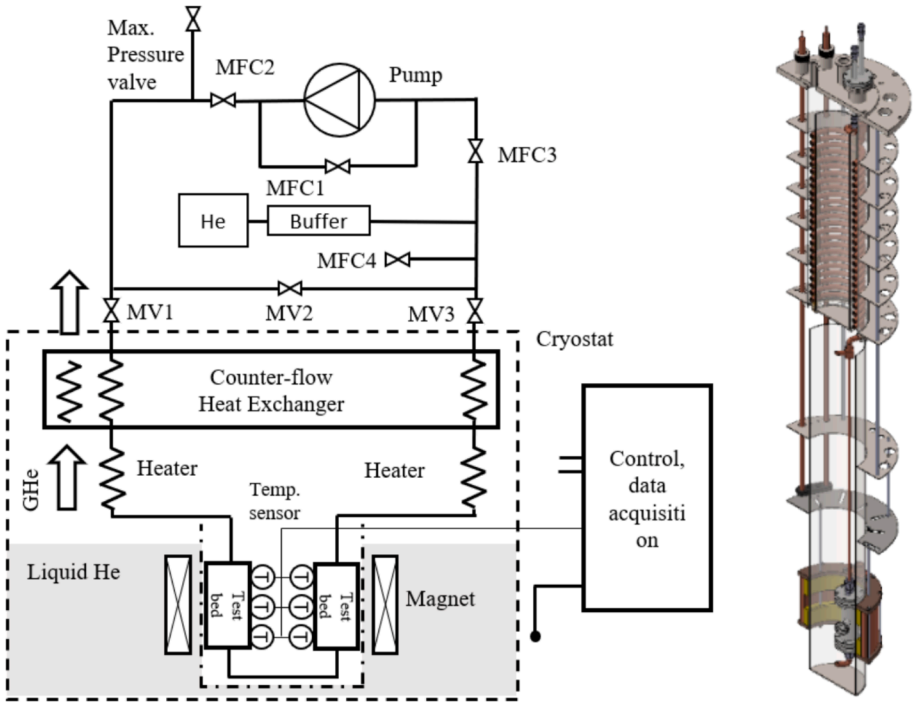

Fig. 6. Schematic of apparatus and data acquisition system (left), the portion enclosed by dashed lines is inside a cryostat. Cryostat side of the test stand (center). Schematic of the heat exchanger (right)

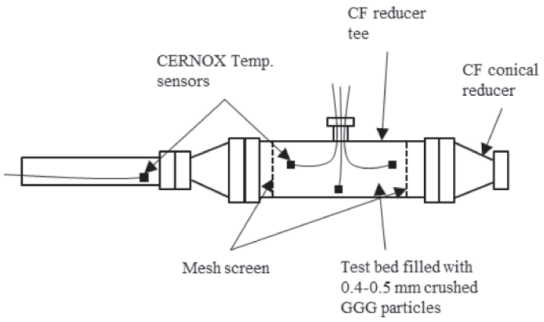

	Packed Bed 1	Packed Bed 2
Length	125 mm.	
Diameter	35 mm.	
Material	$ErAl_2$	GGG
Mass	346.51 g	409.87 g
Particle Diameter	0.45 mm.	0.48 mm.
Shape factor	0.95	0.95
Porosity	0.45	0.45
Instrumentation	4 CERNOX 3 inside the packed bed (x=0, x=L/2, x = L) 1 in the housing wall (x=L/2)	

Fig. 7. Schematic of the GGG packed bed showing temperature sensors positions.

Table 2
Nomenclature for each packed bed instrumentation

	PB1: $ErAl_2$	PB2: GGG
Inlet Temperature	BP1	BP2
Sensor 1 (x=0)	MC1	MC4
Sensor 2 (x=L/2)	MC2	MC5
Sensor 3 (x=L)	MC3	MC6
Wall Sensor	W1	W2

different materials during the same set of experiments. The helium gas goes inside a cryostat and is cooled down in a 3-fluid heat exchanger, rejecting heat to the outgoing helium gas, and to the evaporated helium from the liquid helium bath where the magnet is submerged. A heater controls the temperature at the inlet of each packed bed.

Inside the test bed there is the magnetocaloric material, crushed into particles of small diameter (less than 1 mm.), positioned in a packed bed. Two MCMs have been selected: Gadolinium Gallium Garnet, GGG or $Gd_3Ga_5O_{12}$, and Erbium Aluminum (II), $ErAl_2$ (see Fig. 7).

The results presented in the following sections follows the same nomenclature, the tests of the $ErAl_2$ start with a 1, and the tests of the GGG start with a 2. Table 2 shows the nomenclature of the instrumentation for each packed bed.

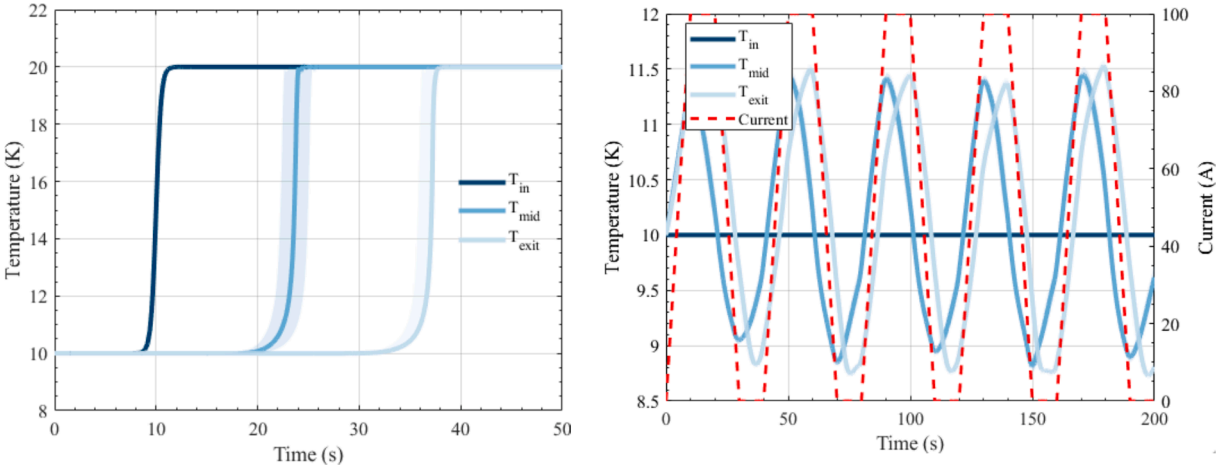

Fig. 8. Example of the temperature evolution during a single blow test (left), and example of a ramping rate test, where a series of 5 trapezoidal magnetic field waveforms is applied to the regenerator while maintaining a constant inlet temperature and mass flow.

4.2. Experimental procedure: Thermal and magnetic tests

The experimental tests are targeted at validating the model presented in the previous section. In this work two types of tests have been performed: thermal tests based on the single blow method, and magnetic tests.

The single-blow testing technique is a transient method used to characterize heat exchangers, particularly regenerators like packed beds. It originated from early studies by Anzelius, Nusselt, Hausen, and Schumann on transient heat transfer between a porous medium and a fluid, and it was first applied by Furnas (1932) for measuring heat transfer coefficients [31]. Comprehensive reviews of these developments are available in the literature [32–34].

This technique involves introducing a sudden change in the temperature of the working fluid at the inlet of the heat exchanger and then observing how this temperature pulse propagates through the system. The transient response of the system is analyzed to determine the heat transfer characteristics, such as the heat transfer coefficient and the thermal capacity of the matrix.

The next group of tests, denominated magnetic tests, consist of applying a cycle of trapezoidal magnetic fields waveforms with different ramping rates, while maintaining constant conditions at the inlet of the packed bed: constant temperature and mass flow rate.

Fig. 8 shows a simulation example of a single-blow test (left) and a magnetic test (right) performed in the present study.

4.2.1. Testing boundary conditions

The following boundary conditions are applied for the resolution of the numerical model, and its comparison against the measured data:

$$T_f(x=0,t) = T_{MC1}(t) \tag{23}$$

$$\frac{\partial T_f}{\partial x}(x=L) = \frac{\partial T_s}{\partial x}(x=0) = \frac{\partial T_s}{\partial x}(x=L) = 0 \tag{24}$$

$$\dot{m}_f(x=0,t) = \dot{m}_{MC1}(t) \tag{25}$$

$$p_f(x=0,t) = p_{MC1}(t) \tag{26}$$

$$\frac{\partial \dot{m}_f}{\partial x}(x=L) = \frac{\partial p_f}{\partial x}(x=L) = 0 \tag{27}$$

$$B(t,x) = B_{nom}(x)^* \frac{I(t)}{I_{nom}} \tag{28}$$

The inlet temperature $T_{MC1}(t)$, the mass flow $\dot{m}_{MC1}(t)$, pressure $p_{MC1}(t)$, and current $I(t)$, are all obtained through real-time data acquisition from the instrumentation. Equation (28) relates the magnet current and test bed magnetic field as function of time and axial position. The current and magnetic field are approximately related by a 100 A to 1 T ratio. More details about the magnet characteristics are given in [30].

5. Results and discussions

5.1. Data reduction procedure

Data reduction techniques play a pivotal role in the analysis of experimental data obtained from the tests. We identify two primary approaches to data reduction: the curve-matching method and the variable-reduction method. In this work the curve-matching method will be applied.

The curve matching method compares entire predicted and measured exit fluid temperature response curves. This method requires more computational effort and is sensitive to inaccuracies in modeling inlet conditions or heat transfer effects.

Ambient losses were modeled as: $Q_{loss} = h_{amb}A_w(T_w - 4.2)$, where h_{amb} is the heat transfer coefficient between the wall and ambient. A value of 4.2 K was set as cold source temperature.

The parameter h_{amb} was optimized to minimize the residuals between the measured and predicted temperatures, using fluid measurements at $x = L/2$ (i = 2) and $x = L$ (i = 3), as well as wall measurements from t = 0 to t = t_{end}:

$$R = \sum_{i=2}^{i=3}\left[\sum_{t=0}^{t=t_{end}}\left(T_{f,t,th} - T_{f,t,exp}\right)\right]^{\frac{1}{2}} + \left[\sum_{t=0}^{t=t_{end}}\left(T_{w,t,th} - T_{w,t,exp}\right)\right]^{1/2} \tag{29}$$

Furthermore, to evaluate the goodness of the fitting, in addition to the residuals, the combined Normalized Root Mean Square Error (NMRMSE) is computed as follows:

$$CombinedNRMSE = \frac{\sqrt{\sum_{i=1}^{N}\sum_{j=1}^{n_i}\left(T_{ij} - \widehat{T}_{ij}\right)^2}}{\frac{1}{N}\sum_{i=1}^{N}\left(T_{max,i} - T_{min,i}\right)} \tag{30}$$

where N is the number of temperature datasets (e.g., MC1, MC2, MC3, wall temperature), n_i is the number of data points in the i-th dataset, T_{ij} is experimental value at the j-th time point in the i-th dataset, $\widehat{T}_{ij}$ is the theoretical value at the j-th time point in the i-th dataset, and $T_{max,i}$ and $T_{min,i}$ are the maximum and minimum values of the experimental data in the i-th dataset.

Table 3
Single blow data test information table

Test Run		B (T)	Mass Flow (g/min)	NRMSE
SB11	$ErAl_2$	0	10	0.1385
SB13	$ErAl_2$	2	10	0.0413
SB15	$ErAl_2$	0	6	0.1434
SB17	$ErAl_2$	2	6	0.0585
SB21	GGG	0	10	0.1651
SB23	GGG	2	10	0.2782
SB25	GGG	0	6	0.2281
SB27	GGG	2	6	0.1747

5.2. Results and analysis

5.2.1. Thermal tests: Single blow tests

The single-blow tests conducted at liquid helium temperatures were performed at the lowest achievable temperature for the test stand, approximately 5 to 6 K. In all instances, hot blows were executed, as generating cold blows proved challenging due to the difficulty in achieving a steady-state temperature across the entire packed bed, primarily because of heat losses to the ambient environment.

Table 3 provides the specific characteristics of each test run, where two key variables were adjusted: the magnetic field and the mass flow rate.

For the $ErAl_2$ case, the model appears to work reasonably well. The NRMSE indicates reasonably low error across all cases. However, the graphical comparison shows certain discrepancies. Fig. 9 illustrates the results from two $ErAl_2$ tests.

The comparison of SB11 reveals a noticeable discrepancy between the experimental and theoretical results, particularly regarding the wall temperature. This suggests the presence of additional heat loss mechanisms in the test bed, most likely due to heat conduction through the walls and two-dimensional effects, such as radial conduction, which are not accounted for in the developed model. However, these factors alone cannot fully explain the divergence observed in the evolution of the packed bed temperature, as heat losses generally slow down the thermal response of the packed bed. By contrast, in SB13, the measured temperature (MC2-Exp) exhibits a faster response than predicted by the model. Several factors could account for this divergence:

First, inaccuracies in the thermophysical properties of $ErAl_2$ may play a role. As discussed in the previous section, discrepancies exist in the literature regarding the properties of this material. Variations in the actual entropy values could partially explain the observed differences. Additionally, the entropy has a significant dependence on the magnetization direction. For instance, it has been reported that the magnetocaloric effect is more pronounced along the easy magnetization direction (<1,1,1>) compared to other directions (<1,1,0> or <1,0,0>). In this study, an average set of material properties was used under the assumption that particles were randomly oriented. However, this assumption may not hold if particles distribution was not sufficiently arbitrary. Another potential source of divergence lies in property changes during the preparation of the packed bed. A similar phenomenon was reported by Yamamoto et al. [35], who observed alterations in $ErCo_2$'s magnetocaloric properties during atomization (100–500 μm particle size). They attributed these changes to their specific atomization process—electrode induction melting gas atomization (EIGA)—which involves substantial heating of the material. Two studies have shown a similar effect in $ErAl_2$: Yamamoto et al. [36] shows slight differences in MCE properties of PIT $ErAl_2$ wires due to the magnetic anisotropy produced by the PIT process, and in Prusty et al. [37] reports that the melt-spun process introduced variations into the material MCE properties. In the present study, such effects are unlikely to have significantly influenced $ErAl_2$, as no substantial temperature changes occurred during its atomization process. Nevertheless, it remains unclear how the original material was processed prior to its use in the present study, and specific measurements are needed to confirm this possibility.

A second potential source of error arises from the lack of local measurements for mass flow and pressure. Although all sensors were placed near the packed bed for ambient temperature measurements, the cryogenic assembly recorded mass flow and pressure in the ambient temperature circuit. Local fluid properties may therefore differ substantially, and the assumed boundary conditions may not fully capture actual system behavior.

A third option is the inaccurate positioning of the temperature sensors along the packed bed, which can also contribute to discrepancies. For instance, a larger distance between MC2 and MC3 might explain the

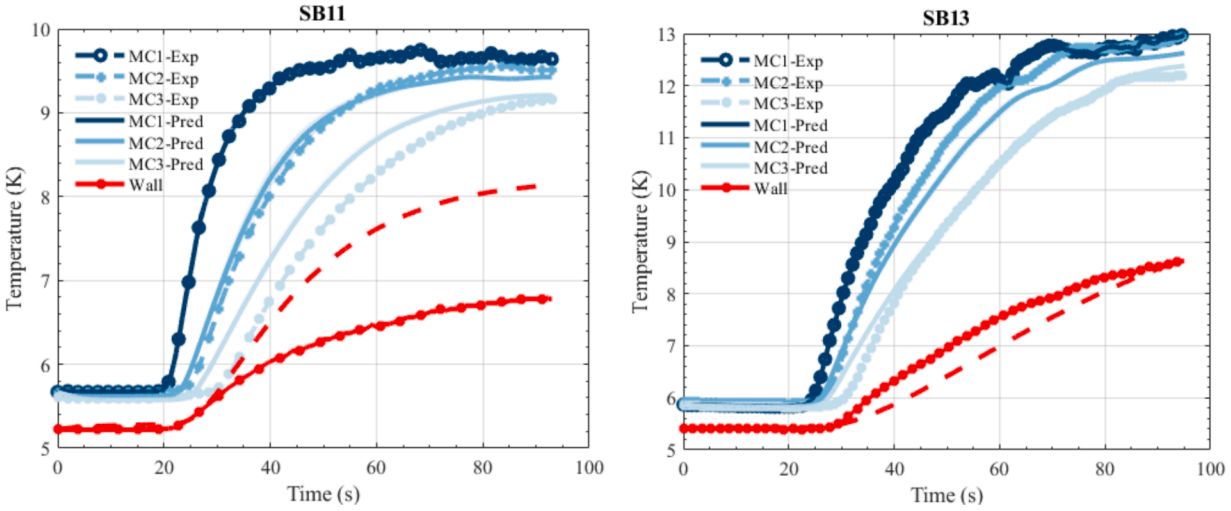

Fig. 9. SB11-SB14 tests: single blow test of $ErAl_2$ with mass flow of 10–6 g/min for magnetic fields of 0–2 T, and comparison against improved model.

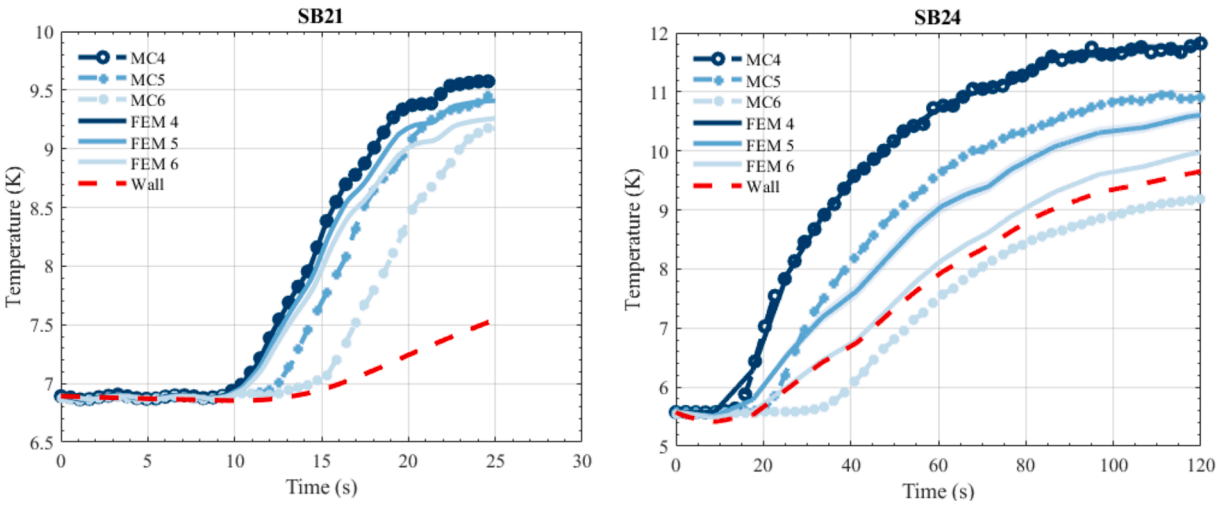

Fig. 10. SB21-SB24 tests: single blow test of GGG with mass flow of 10–6 g/min for magnetic fields of 0–2 T, and comparison against improved model.

larger temperature differences. This possibility was evaluated, and the predicted temperatures in the figures include a shaded region representing a ± 5 % positioning error.

Additional unmodeled effects may further undermine accuracy. Examples include radial conduction within the packed bed and surrounding wall, nonuniform flow profiles with pronounced entrance and exit influences, and variations in porosity throughout the bed.

Next is the analysis of the GGG single blow test results. Fig. 10 shows the results from GGG testing. The analysis of GGG presents additional challenges, since the temperature sensor measuring the wall temperature malfunctioned during testing, necessitating the use of heat loss data from previous tests. This substitution introduces a degree of uncertainty into the results.

The model's predictions for GGG exhibit clear discrepancies, particularly at low magnetic fields. These deviations are likely due to the low specific heat capacity of GGG in this temperature range, which increases its sensitivity to external influences such as ambient losses and entrance effects. As the magnetic field increases, resulting in a higher specific heat capacity, the model's accuracy improves slightly, but the fit remains suboptimal. This highlights the need for further refinement of the model to better capture the thermal behavior of GGG under varying conditions.

Similar conclusions to the $ErAl_2$ tests can be drawn. First, accurate property measurements of magnetocaloric materials before and after preparation (e.g., atomization) are essential to reduce uncertainties in modeling and experimental analysis. Second, test bed designs must be refined to minimize ambient losses and entrance effects, which currently introduce notable discrepancies between measured and predicted results. Third, adding localized measurements of mass flow and pressure would enhance data reliability and facilitate more precise validation. Furthermore, developing models that account for radial effects and axial dispersion could improve predictive accuracy across a broader range of conditions.

Table 4
$ErAl_2$ magnetic test results information table

Title	B (T)	dI/dt (A/s)	T_{start} (K)	Mass Flow (g/min)	NRMSE
VT110	1	20	6	10	0.4486
VT111	2	20	6	10	0.2667
VT112	3	20	6	10	0.1410
VT113	1	20	10	10	0.2139
VT114	2	20	10	10	0.2113
VT115	3	20	10	10	0.1665
VT116	1	20	15	10	0.5346
VT117	2	20	15	10	0.4905
VT118	3	20	15	10	0.4341

5.2.2. *Magnetic tests*

The results analysis section follows a structure similar to that of the previous sections: a table is presented containing the fitting results, which is accompanied by a graphical comparison between the model predictions and the measured data.

The data presented in Table 4 provide several key observations. First, the NRMSE for most tests, with the exception of those conducted at 15 K, falls within the range of 0.15 to 0.25. In contrast, tests performed at 15 K exhibit poorer agreement, with NRMSE values ranging from approximately 0.4 to 0.55. This fact supports previous observation suggesting that $ErAl_2$ properties may be inaccurate, especially near the Curie temperature, which as reported in Fig. 5 is where properties from the literature significantly diverged.

Fig. 11 illustrates a comparison between the model predictions and experimental measurements for selected tests. A reasonable agreement is evident in these cases. For figure clarity the current evolution is not displayed.

Table 5 presents the results of the GGG magnetic tests. The results of

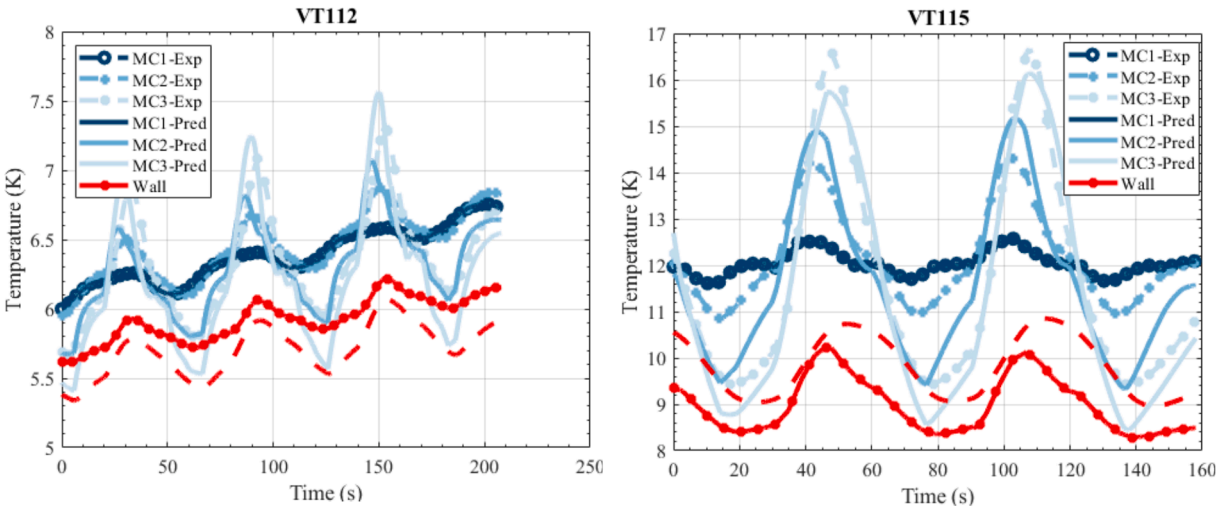

Fig. 11. Comparison of experimental and theoretical values from $ErAl_2$ magnetic tests.

Table 5
GGG magnetic test results information table

Title	B (T)	dI/dt (A/s)	T_{start} (K)	Mass Flow (g/min)	NRMSE
VT25	2	20	10	6	0.5572
VT26	3	20	10	6	0.3428
VT214	2	20	10	10	0.0890
VT215	3	20	10	10	0.1222
VT220	4	20	10	10	0.1826
VT221	2	20	10	15	0.1880

the GGG testing are mixed. The discrepancies are more pronounced in the low mass flow rate (low Reynolds) region. This discrepancy suggests that the flow may not have fully developed. A plausible explanation for these observations is that the flow transitions toward a laminar regime as the Reynolds number decreases. In such conditions, axial and radial dispersion effects may become more significant than predicted, and may exert a greater influence on flow dynamics. In either case, more testing is needed to confirm this observations.

Fig. 12 illustrates the comparison for the experimental and model prediction.

6. Conclusions

The testing of $ErAl_2$ and GGG packed beds has provided valuable insights into their magnetocaloric properties and the associated challenges of modeling their thermal behavior at cryogenic temperatures. The experimental results revealed discrepancies between measured and predicted temperature responses, which were attributed to several factors, including ambient losses, material property variations, and

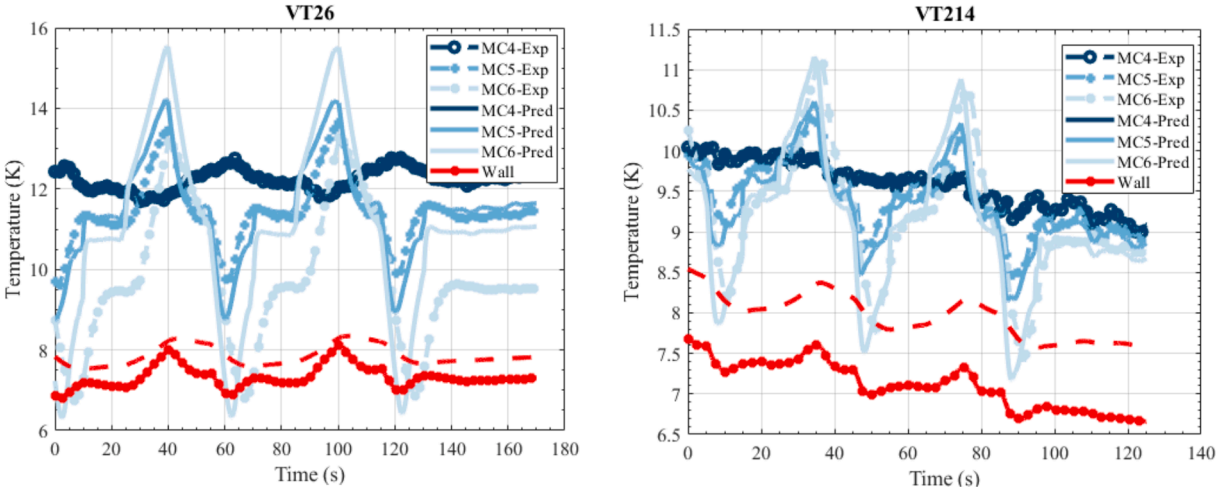

Fig. 12. Comparison of experimental and theoretical values from GGG magnetic tests.

entrance/exit effects.

These findings underscore the need for further refinement of both experimental setups and numerical models. Improved local measurements of pressure and mass flow within the packed bed would enhance data reliability and model accuracy. Additionally, incorporating more advanced models that account for axial dispersion and radial effects is essential for better capturing the dynamics of cryogenic magnetocaloric systems. Comprehensive measurements of magnetocaloric properties across a broader range of temperatures and magnetic fields are also critical for reducing uncertainties in material behavior predictions.

Addressing these challenges will contribute to developing more accurate and reliable models for magnetocaloric refrigeration systems, advancing the field of cryogenic cooling for high-temperature superconductor applications.

CRediT authorship contribution statement

Carlos Hernando: Writing – review & editing, Writing – original draft, Visualization, Validation, Supervision, Software, Resources, Project administration, Methodology, Investigation, Funding acquisition, Formal analysis, Data curation, Conceptualization. **Javier Munilla:** Writing – review & editing, Validation, Supervision, Project administration, Funding acquisition, Conceptualization. **Luis García-Tabarés:** Writing – review & editing, Visualization, Supervision, Funding acquisition, Conceptualization.

Declaration of competing interest

The authors declare the following financial interests/personal relationships which may be considered as potential competing interests: Carlos Hernando reports financial support was provided by Community of Madrid. Carlos Hernando reports financial support was provided by European Union. If there are other authors, they declare that they have no known competing financial interests or personal relationships that could have appeared to influence the work reported in this paper.

Data availability

Data will be made available on request.

References

[1] Chakravarthy VS, Shah RK, Venkatarathnam G. A review of refrigeration methods in the temperature range 4-300 K. J Therm Sci Eng Appl 2011;3(2). https://doi.org/10.1115/1.4003701.

[2] Radebaugh R. Cryocoolers: the state of the art and recent developments. J Phys Condens Matter 2009;21(16):164219. https://doi.org/10.1088/0953-8984/21/16/164219.

[3] Franco V, Blázquez JS, Ipus JJ, Law JY, Moreno-Ramírez LM, Conde A. Magnetocaloric effect: From materials research to refrigeration devices. Progr Mater Sci 2018;93:112–232. https://doi.org/10.1016/j.pmatsci.2017.10.005.

[4] Brück E. Developments in magnetocaloric refrigeration. J Phys D: Appl Phys, vol. 38, no. 23. IOP Publishing, p. R381, Dec. 07, 2005. doi: 10.1088/0022-3727/38/23/R01.

[5] Gregory F. Nellis, "Magnetically aumented cryogenic refrigeration," University of Wisconsin (Doctoral thesis), 1992. [Online]. Available: https://dspace.mit.edu/handle/1721.1/11482.

[6] Morgan R, Rota C, Pike-Wilson E, Gardhouse T, Quinn C. The modelling and experimental validation of a cryogenic packed bed regenerator for liquid air energy storage applications. Energies 2020;13(19). https://doi.org/10.3390/en13195155.

[7] Nielsen KK, et al. Review on numerical modeling of active magnetic regenerators for room temperature applications. Int J Refrig, 2011;34(3):603–16. https://doi.org/10.1016/J.IJREFRIG.2010.12.026.

[8] Diamantopoulos T, Matteuzzi T, Bjørk R. 1D models of an active magnetic regeneration cycle for cryogenic applications. Int J Refrig, Nov. 2024;167:246–56. https://doi.org/10.1016/J.IJREFRIG.2024.08.011.

[9] Skeel RD, Berzins M. A method for the spatial discretization of parabolic equations in one space variable. SIAM J Sci Stat Comput, Jan. 1990;11(1):1–32. https://doi.org/10.1137/0911001.

[10] Wakao N, Kaguei S, Funazkri T. Effect of fluid dispersion coefficients on particle-to-fluid heat transfer coefficients in packed beds: Correlation of nusselt numbers. Chem Eng Sci, Jan. 1979;34(3):325–36. https://doi.org/10.1016/0009-2509(79)85064-2.

[11] Rohsenow WM, Hartnett JP, Cho Yi. Handbook of Heat Transfer, no. 1. McGraw-Hill Education, 1998. Accessed: Jan. 11, 2025. [Online]. Available: https://www.accessengineeringlibrary.com/content/book/9780070535558.

[12] Ergun S. Fluid Flow Through Packed Columns. Chem Eng Prog, 1952;48:89.

[13] Kaviany M. Principles of Heat Transfer in Porous Media. in Mechanical Engineering Series. New York, NY: Springer New York, 1995. doi: 10.1007/978-1-4612-4254-3.

[14] Hadley GR. Thermal conductivity of packed metal powders. Int J Heat Mass Transf, Jun. 1986;29(6):909–20. https://doi.org/10.1016/0017-9310(86)90186-9.

[15] "Thermophysical Properties of Fluid Systems." Accessed: Jan. 04, 2025. [Online]. Available: https://webbook.nist.gov/chemistry/fluid/.

[16] Barclay JA, Stewart WF, Overton WC, Candler RJ, Harkleroad OD. Experimental results on a low-temperature magnetic refrigerator. Adv Cryog Eng, 1986;31:743–52. https://doi.org/10.1007/978-1-4613-2213-9_84.

[17] Numazawa T, Hashimoto T, Nakagome H, Tanji N, Horigami O. The Helium Magnetic Refrigerator II: Liquefaction Process and Efficiency. Adv Cryog Eng, 1984;29:589–96. https://doi.org/10.1007/978-1-4613-9865-3_67.

[18] Nakagome H, Kuriyama T, Ogiwara H, Fujita T, Yazawa T, Hashimoto T. Reciprocating Magnetic Refrigerator for Helium Liquefaction. Adv Cryog Eng, 1986;31:753–62. https://doi.org/10.1007/978-1-4613-2213-9_85.

[19] G. Nellis, "Stirling-magnetic cryocooler," Massachusetts Institute of Technology, 1997. Accessed: Jan. 03, 2025. [Online]. Available: https://www.researchgate.net/publication/35035457_Stirling-magnetic_cryocooler.

[20] C. P. (Carl P. Tausczik, "Magnetically active regeneration," Massachusetts Institute of Technology, 1986. Accessed: Jan. 04, 2025. [Online]. Available: https://dspace.mit.edu/handle/1721.1/14917.

[21] Bézaguet A, et al. Design and construction of a static magnetic refrigerator operatingbetween 1.8 K and 4.5 K. Cryogenics (Guildf) Jan. 1994;34(SUPPL. 1):227–30. https://doi.org/10.1016/S0011-2275(05)80049-9.

[22] Steyert WA. Final report on NRIP-funded magnetic refrigerator development project, July 1, 1975–October 1, 1977. [New Research Initiatives Program (NRIP)], Los Alamos Scientific Laboratory, Los Alamos, NM, Feb. 1978. doi: 10.2172/5170870.

[23] de Oliveira NA, von Ranke PJ. Theoretical aspects of the magnetocaloric effect. Phys Rep, Apr. 2010;489(4–5):89–159. https://doi.org/10.1016/J.PHYSREP.2009.12.006.

[24] Murphy RW. Thermodynamic property evaluation and magnetic refrigeration cycle analysis for gadolinium gallium garnet, Dec. 1994, doi: 10.2172/10114667.

[25] Mastrup FN, Price KD. Thermodynamic Performance Measurements of a 10K, Ga3Ga5O12 Paramagnetic Stage. Proc Interag Meet Cryocoolers 1988:149–59.

[26] Dai W, Gmelin E, Kremer R. Magnetothermal properties of sintered Gd3Ga5O12. J Phys D Appl Phys, Apr. 1988;21(4):628–35. https://doi.org/10.1088/0022-3727/21/4/014.

[27] Schelp W, Drewes W, Leson A, Purwins HG. Low temperature heat capacity of some heavy REA12 compounds (RE = Tb, Dy, Er and Tm) in a magnetic field. J Phys Chem Solids Jan. 1986;47(9):855–61. https://doi.org/10.1016/0022-3697(86)90056-9.

[28] Inoue T, Sankar SG, Craig RS, Wallace WE, Gschneidner Jr KA. Low temperature heat capacities and thermal properties of $DyAl_2$, $ErAl_2$ and $LuAl_2$. J Phys Chem Solids 1977;38(5):487–97. https://doi.org/10.1016/0022-3697(77)90182-2.

[29] Slack GA, Oliver DW. Thermal Conductivity of Garnets and Phonon Scattering by Rare-Earth Ions. Phys. Rev. B Jul. 1971;4(2):592. https://doi.org/10.1103/PhysRevB.4.592.

[30] Lopez De Toledo CH, et al. Cryogenic Test Stand for Characterization of Magnetocaloric Materials. IEEE Trans Appl Supercond, May 2024;34(3):1–5. https://doi.org/10.1109/TASC.2024.3370126.

[31] Furnas CC. Heat Transfer from a gas Stream to bed of Broken Solids. Ind Eng Chem, Jan. 1930;22(1):26–31. https://doi.org/10.1021/IE50241A007/ASSET/IE50241A007.FP.PNG_V03.

[32] Krishnakumar K, John AK, Venkatarathnam G. A review on transient test techniques for obtaining heat transfer design data of compact heat exchanger surfaces. Exp Therm Fluid Sci, May 2011;35(4):738–43. https://doi.org/10.1016/j.expthermflusci.2010.12.006.

[33] Pucci PF, Howard CP, Piersall CH. The Single-Blow Transient Testing Technique for Compact Heat Exchanger Surfaces. J Eng Power Jan. 1967;89(1):29–38. https://doi.org/10.1115/1.3616604.

[34] Chang ZC, Hung MS, Ding PP, Chen PH. Experimental evaluation of thermal performance of Gifford-McMahon regenerator using an improved single-blow model with radial conduction. Int J Heat Mass Transf, Feb. 1998;42(3):405–13. https://doi.org/10.1016/S0017-9310(98)00186-0.

[35] Yamamoto TD, Saito AT, Takeya H, Terashima K, Numazawa T, Takano Y. Tunable magnetic and magnetocaloric properties by thermal annealing in ErCo2 atomized particles. J Alloys Compd, Feb. 2023;935:168040. https://doi.org/10.1016/J.JALLCOM.2022.168040.

[36] Yamamoto TD, Takeya H, Iwasaki S, Terashima K, De Castro PB, Numazawa T, Takano Y. Magnetic entropy change of ErAl2 magnetocaloric wires fabricated by a powder-in-tube method. J Phys D. Appl Phys 2019;53(9):095004. https://doi.org/10.1088/1361-6463/ab5c71.

[37] Prusty MM, et al. Magnetocaloric effect in melt-spun rare earth intermetallic compound ErAl2. AIP Adv, Mar. 2022;12(3):35145. https://doi.org/10.1063/9.0000358.